RSC Advances

PAPER

View Article Online
View Journal | View Issue

Cite this: RSC Adv., 2017, 7, 50307

Self-crosslink assisted synthesis of 3D porous branch-like Fe_3O_4/C hybrids for high-performance lithium/sodium-ion batteries†

Ning Wang,[a] Qinglei Liu,*[a] Yue Li,[a] Jichao Chen,[b] Jiajun Gu,[a] Wang Zhang[a] and Di Zhang[a]

Received 23rd August 2017
Accepted 13th October 2017

DOI: 10.1039/c7ra09348a

rsc.li/rsc-advances

A facile and effective self-crosslink assisted strategy is developed to fabricate 3D porous branch-like Fe_3O_4/C hybrids as high-performance anode materials for lithium ion batteries (LIBs) and sodium ion batteries (NIBs). Trivalent iron ions (Fe^{3+}) are used to directly crosslink with biopolymer alginate to form nanoscale branch-like Fe-alginate hybrid nanostructures, which are converted to porous Fe_3O_4/C hybrids *via* a simple carbonization process. The resulting hybrids feature ultrafine active nanoparticles (~5 nm), wrapping by thin graphitic layers, hierarchically nanoscale porous channels, and interconnected robust graphitic frameworks. Applying these in the anodes of LIBs, these structural features enable the hybrids to deliver high capacities of 974 and 570 mA h g^{-1} at 0.1 and 2 A g^{-1}, respectively, and excellent cyclic stability with capacity retention of 98% after 200 cycles at 0.1 A g^{-1}. In NIBs, reasonable capacities of 339 and 138 mA h g^{-1} are obtained at 0.05 and 5 A g^{-1}, respectively. The high performance demonstrates the promising potential of the hybrids in next generation anodes for LIBs and NIBs.

1. Introduction

Li-ion batteries (LIBs) have been widely used in consumer electronics and electric vehicles because of their high energy density, long cycle lifespan and environmental friendliness.[1–3] However, the ever growing huge demand for electrical energy storage (EES) devices, as well as the limited reserves and the relatively high cost of lithium, make the future of LIBs very challenging. To alleviate these problems, Na-ion batteries (NIBs), as alternatives for LIBs, are now drawing increasing attention from scientists, due to the analogous electrochemical properties of sodium and lithium, but much more natural abundance and lower cost of sodium (~10^3 the reserve and ~1/20 the price of lithium).[4–6] To meet the huge commercial requirements, both LIBs and NIBs need to improve their specific capacities and cycling life. As the performance of batteries are mostly determined by the electrode materials, developing high-performance electrode materials available for both LIBs and NIBs are of great importance.

During the past two decades, various of electrode materials including porous carbons,[7–11] metal oxides like SnO_2,[12–15] MnO_2,[16–18] Fe_3O_4,[19,20] Co_3O_4,[21,22] and other materials[23–27] have been investigated. Among these reported materials, Fe_3O_4 has been considered as one of the most promising anode materials for LIBs and NIBs, because of its high theoretical capacity (926 mA h g^{-1} for both LIBs and NIBs), nontoxic nature, earth abundance and low cost.[28–33] However, when applied in practical use, Fe_3O_4-based anode materials usually suffer from severe volume expansion and particle pulverization during charge–discharge cycling, which lead to low rate performance and poor cycling stability.[34–36] To achieve higher rate and better cycling performance, various strategies have been developed to improve the structural integrity and electronic conductivity of Fe_3O_4-based electrode materials. So far, the most recognized strategies are to optimize the particle size of Fe_3O_4 (ref. 37–39) and to induce porous carbon materials as conductive frameworks.[20,34–36,40,41] For example, in the field of LIBs, Chen and coworkers[42] reported a two-step method to encapsulate Fe_3O_4 nanoparticles (~5 nm) in mesoporous carbon spheres. The obtained Fe_3O_4@C showed capacity of 580 and 271 mA h g^{-1} at 0.5 and 10 A g^{-1}, respectively. Wei and coworkers[34] reported a hydrothermal method to assemble Fe_3O_4 nanospheres (~200 nm) with graphene. The resulted hybrid exhibited good rate performance with capacity of 802 and 363 mA h g^{-1} at 0.15 and 4.8 A g^{-1}, respectively, as well as improved cycling performance of more than 100% retention after 150 cycles at 0.093 A g^{-1}. Li and coworkers[43] used a multistep protocol to load Fe_3O_4 (~10 nm) on graphene nanoribbons. The as-prepared hybrid delivered an enhanced cycling stability with capacity retention of 708 mA h g^{-1} after 300 cycles at 0.1 A g^{-1}. Despite of many attempts, it is still challenging to fulfill the huge demand for the market of electrical vehicles. Rational design and facile

---

[a] State Key Laboratory of Metal Matrix Composites, Shanghai Jiao Tong University, 800 Dongchuan Road, Shanghai, 200240, P. R. China. E-mail: liuqinglei@sjtu.edu.cn; Fax: +86 21 34202634; Tel: +86 21 34202634

[b] CRRC Industrial Institute Co., Ltd, China

† Electronic supplementary information (ESI) available. See DOI: 10.1039/c7ra09348a

fabrication of Fe_3O_4-based materials with excellent high-rate performance and long cycling life are still in urgent need.

Here, we present a novel and facile strategy to fabricate 3D porous branch-like Fe_3O_4/C nanohybrids for anode materials of LIBs and NIBs by a one-step carbonization of self-crosslinked Fe-alginate. Recently, the bio-copolymer alginate, composed of α-L-guluronate (G) and β-D-mannuronate (M) blocks,[44,45] has been reported to have the nature of adsorbing divalent metal cations through an assembly crosslinking reactions between the G blocks and divalent metal cations.[46] In this work, we find that the trivalent iron ions can also self-crosslink with alginate, and especially the carbonized product of Fe-alginate exhibited a unique 3D integrated branch-like structure due to the odd valence of iron ions. The branch-like hybrid structures not only own nanosized electrochemical active particles and mesoporous channels, but also possess favorable robust and interconnected graphitized carbon frameworks, which are beneficial to alleviate the volume change induced strain and stress during cycling, so as to maintain the structural integrity and cyclic stability. The obtained Fe_3O_4/C hybrid, with high load (58.8 wt%) of nano-sized (~5 nm) Fe_3O_4 perfectly embedded in the conductive (partially graphitized) and mesoporous (high specific surface area of 389.8 $m^2\ g^{-1}$) carbon matrix, exhibited excellent performance as the anode of LIBs and NIBs. For the LIBs, the Fe_3O_4/C hybrid anode delivered high capacities of 974 and 570 mA h g^{-1} at 0.1 and 2 A g^{-1}, respectively, and excellent cyclic stability with capacity retention of 98% after 200 cycles at 0.1 A g^{-1}. As for the NIBs, reasonable capacities of 339 and 138 mA h g^{-1} were obtained at 0.05 and 5 A g^{-1}, respectively.

2. Experimental

2.1. Material synthesis

The Fe_3O_4/C hybrid was synthesized by a simple carbonization of crosslinked Fe-alginate assemblies, as shown in Fig. 1. Typically, 1.5 wt% of sodium alginate aqueous solution were added into 1.5 wt% of ferric trichloride solution, under a volume ratio of 1 : 5. The as-prepared Fe-alginate was freeze-dried for 24 h to remove water. Then the dried Fe-alginate was carbonized at 600 °C for 1 h with N_2 atmosphere to obtain the final Fe_3O_4/C hybrid.

2.2. Material characterization

Scanning electron microscope (SEM) observations were carried out on a FEI field emission microscope. Transmission electron microscope (TEM), high-resolution TEM (HR-TEM) and selected area electron diffraction (SAED) studies were performed on a JEOL JEM-2100F. X-ray diffraction (XRD) was conducted on a Rigaku D/Max-2500 with Cu-Kα radiation. Thermogravimetric analysis (TGA) was studied on a Netzsch TGA instrument from 30 to 800 °C with a heating rate of 10 °C min^{-1} under air. Nitrogen sorption isotherms were measured on a Micromeritics ASAP 2020 at 77 K. Pore size distributions were calculated on the basis of the density function theory (DFT) model. Raman spectra were obtained on a Renishaw in Via-reflex spectrometer with a crystal laser excitation of 532 nm.

2.3. Electrochemical measurement

Electrochemical measurements were carried out in half-cell configurations with lithium and sodium foils as counter electrode. To prepare the working electrodes, active materials, Super P, and poly-(vinyl difluoride) (PVDF) with a weight ratio of 8 : 1 : 1 were mixed uniformly in the solution of *N*-methylpyrrolidone (NMP) to make a slurry. Then the slurry was coated on a copper foil with a thickness of 100 μm. After drying at 110 °C overnight under vacuum, these coated copper foils were cut into disks, pressed at 4 MPa, and dried for another 12 h at 110 °C in vacuum. Then the as-prepared electrodes were transferred into the glove box filled with argon atmosphere for

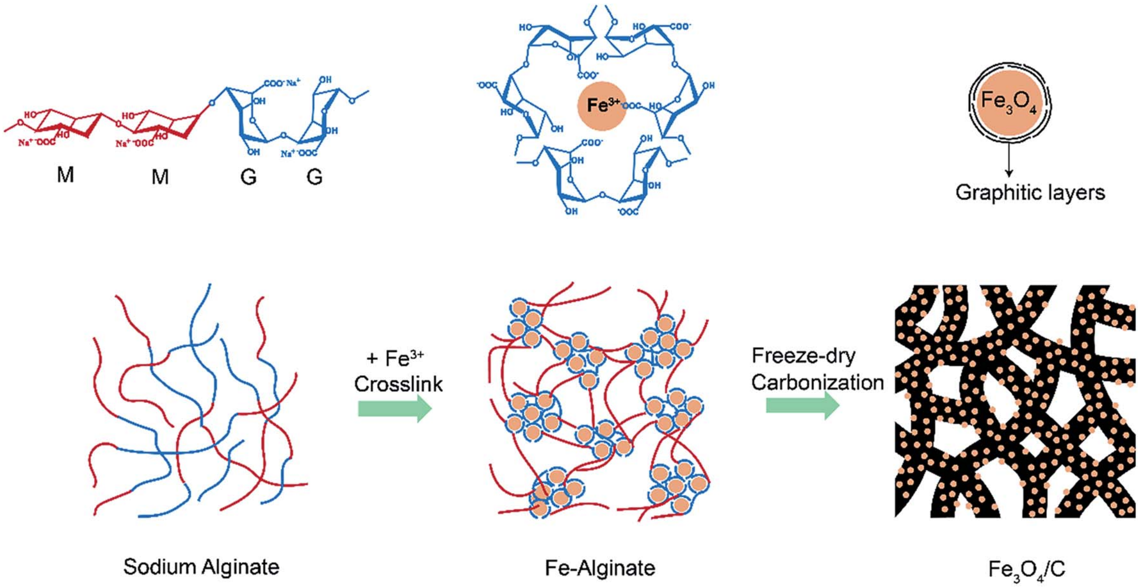

Fig. 1 Schematic of the synthesis process of Fe_3O_4/C hybrid.

half-cell assembling. For lithium-half cells, lithium foil was used as the counter electrode, Celgard 2500 was used as the separator, and the electrolyte was a 1 M $LiPF_6$ in ethylene carbonate (EC) and dimethyl carbonate (DMC) (v/v = 1 : 1). For sodium-half cells, sodium foil was used as the counter electrode, glass fibers (GF/D) from Whatman were used as the separator, and the electrolyte was a 1 M $NaClO_4$ solution in ethylene carbonate (EC) and propylene carbonate (PC) (v/v = 1 : 1).

The Galvanostatic charge–discharge (GCD) curves were measured on a Land CT2001A at a voltage window of 0.005–3.0 V. The cyclic voltammetry (CV) with a scan rate of 0.1 mV s^{-1} (0.005–3.0 V) and electrochemical impedance spectroscopy (EIS) with a frequency range of 10 mHz to 100 kHz and ac amplitude of 10 mV were performed on a VMP3 electrochemical working station.

3. Results and discussion

3.1. Microstructures of the Fe_3O_4/C hybrid

The morphology and microstructure of the as-prepared Fe_3O_4/C hybrid were characterized by SEM and TEM measurements, as shown in Fig. 2. The hybrid exhibits a nanoscale branch-like foam structure as a whole, with a lot of pores in it (Fig. 2a). On a larger magnification, these thready branches are not separated but integrated with joints, so as to form an integrated network (Fig. 2b and c), which is crucial to keep the physical stability of electrodes during charge–discharge processes. Fig. 2c shows that the surface of these branches are stacked with dense and uniform nanosized particles. The TEM observations in Fig. 2d and e show that the whole branch-like foam is densely composed of uniform Fe_3O_4 nanoparticles and carbon branches. The HR-TEM image in Fig. 2f shows that these Fe_3O_4 nanoparticles are around 5 nm in diameter, and are wrapped by 2–3 layers of graphitic carbons. These graphitic layers are produced by the catalytic graphitization of Fe particles. During carbonization, the amorphous carbon structures adjacent to Fe particles are transformed into ordered graphitic layers through dissolution-precipitation mechanism.[47] These graphitic layers can buffer the volume change induced stress and facilitate the transfer of electrons to improve the reactive kinetics. This uniform Fe_3O_4/C hybrid structure is produced by self-crosslinking and hardly achieved by normally solution methods.

Fig. 3 shows the chemical component and pore characterization of the Fe_3O_4/C hybrid. The XRD pattern in Fig. 3a shows several peaks at 18.3, 30.1, 35.4, 37.1, 43.1, 56.9, 62.5 and 73.9°, all of which are indexed to the spinel Fe_3O_4 (JCPDS: 19-0629). The broad and short XRD peaks indicate that the Fe_3O_4 particles are nano sized, as verified by TEM images. The TGA curve in Fig. 3b shows sharp weight decrease at 300–500 °C, which is ascribed to the combustion of carbons of the Fe_3O_4/C hybrid ($C + O_2 \rightarrow CO_2$) in air. The remaining weight after 500 °C is provided by Fe_3O_4 nanoparticles and the weight percentage of Fe_3O_4 nanoparticles is thus calculated to be 58.8%. The N_2 adsorption–desorption isotherm in Fig. 3c shows a typical type-IV curve with distinct increase of N_2 adsorption and hysteresis loop at the moderate and high relative pressure. The Fe_3O_4/C hybrid shows a relatively high specific surface area of 389.8 m^2 g^{-1}. The pore size distribution inset in Fig. 3c shows the existence of large number of mesopores and macropores. The mesopores were induced by Fe^{3+} crosslinking, where Fe^{3+} ions

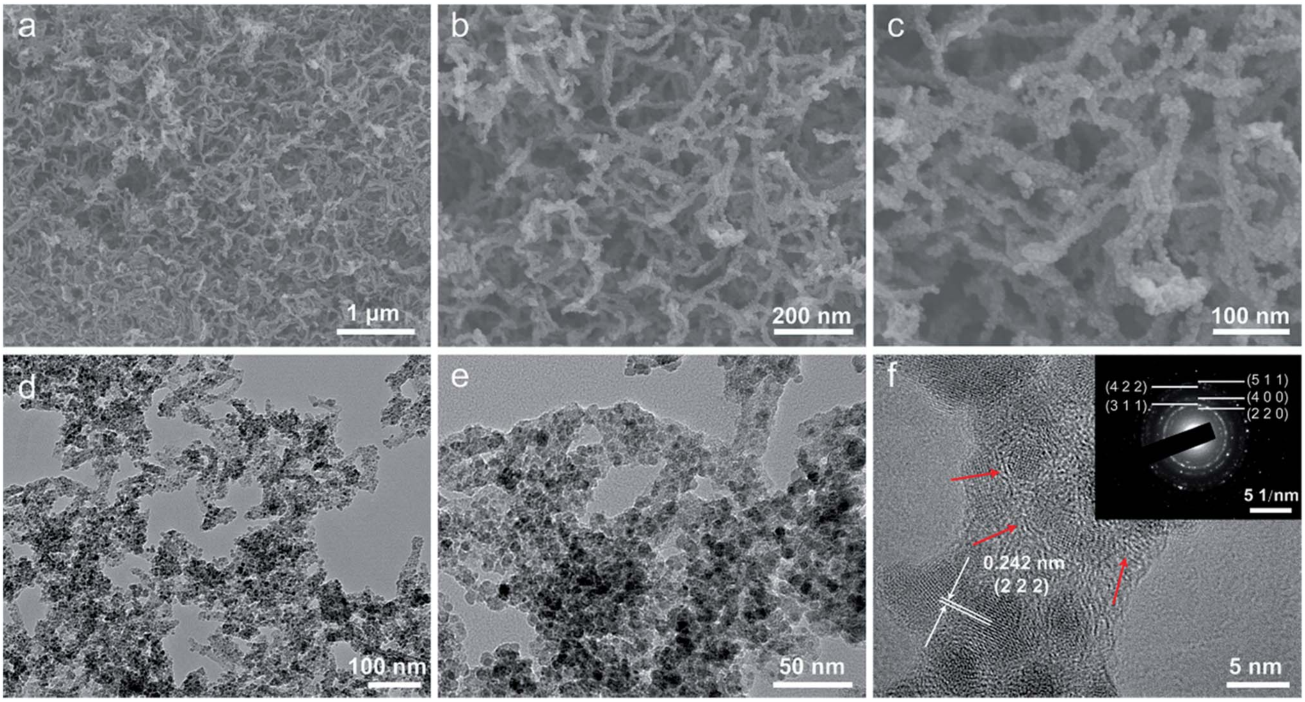

Fig. 2 Morphology of the Fe_3O_4/C hybrid. (a–c) SEM images. (d–f) TEM images.

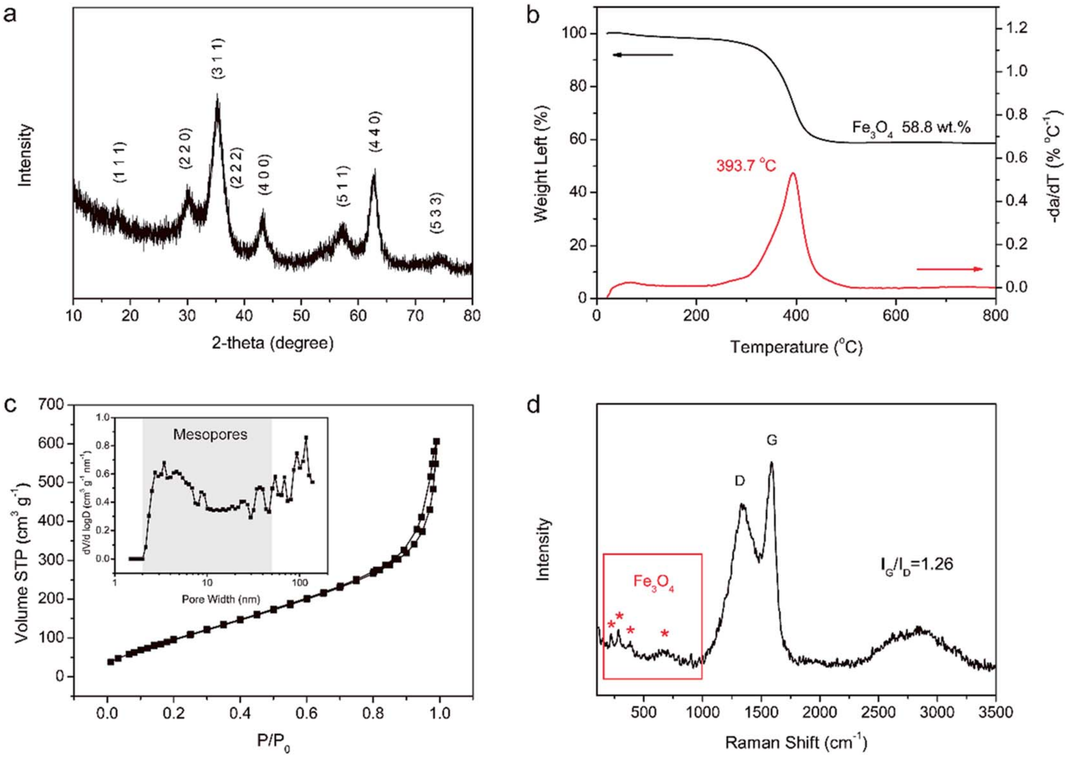

Fig. 3 Chemical component and pore characterization of Fe_3O_4/C hybrid. (a) XRD pattern. (b) TGA curves. (c) N_2 isothermal and pore size distribution. (d) Raman spectrum.

crosslinked with adjacent G blocks in alginate, leaving space among the M blocks. The rearrangement of G/M blocks results in the mesoporous channels around the crosslinked nanostructures. Macropores were mostly produced by the freeze-drying process,[48] as sublimation of ice would leave lot of spaces. This interconnected hierarchical porous structure can facilitate the mass transport and buffer the volume change during the charging/discharging processes when applied as electrodes of LIBs and NIBs.[49–53] Particularly, the mesopores are preferred in NIBs, since the radius of Na^+ (0.102 nm) is larger than that of Li^+ (0.076 nm).[54,55] Raman spectrum in Fig. 3d shows characteristic peaks for both the Fe_3O_4 nanoparticles and the carbon framework. The four weak peaks at 219, 282, 384 and 656 cm^{-1} are ascribed to the Raman active models of Fe_3O_4. The two sharp peaks at 1359 and 1585 cm^{-1} are attributed to the D- and G-band of carbons, respectively. The D-band corresponds to the response from defects and disordered carbons, while the G-band represents the C–C stretching mode of the highly ordered graphitic layers with a sp^2 orbital structure. The I_G/I_D value of Fe_3O_4/C hybrid is as high as 1.26, indicating a high degree of graphitization. Such high degree of graphitization at low carbonization temperature of 600 °C is related to the catalytic graphitization of Fe nanoparticles.[56,57]

3.2. Electrochemical performance of the LIBs

The electrochemical performance of Fe_3O_4/C hybrid was firstly tested in the lithium half-cells. Fig. 4a shows the first three CV curves with scan rate of 0.1 mV s^{-1} at voltage window of 0.005–3 V. In the first discharge, the little peak at 0.96 V and the sharp peak at 0.68 V are related to the formation of solid electrolyte interphase (SEI) film, corresponding to the two-step lithiation reaction of Fe_3O_4 (step 1, $Fe_3O_4 + 2Li^+ + 2e^- \rightarrow Li_2(Fe_3O_4)$; and step 2, $Li_2(Fe_3O_4) + 6Li^+ + 6e^- \rightarrow 4Li_2O + 3Fe$).[35,36] In the following cycles, the only reduction peak at 0.76 V is attributed to the reduction from Fe_3O_4 to Fe. The two peaks at 1.56 and 1.88 V in the charge process are ascribed to the oxidization from Fe to Fe_3O_4. Besides, the sharp reduction peak near 0.1 V and the broad oxidation peak near 0.2 V are ascribed to the insertion/extraction of Li into/from graphitic layers in the carbon matrix.[58] Fig. 4b shows the first three GCD profiles at 0.1 A g^{-1} within voltage range of 0.005–3 V. The GCD profiles match well with the CV curves above. In the first discharge, the short plateau at 1.05 V and the longer plateau at 0.80 V correspond to the two discharge peaks at the first discharge CV curve, indicating the formation of SEI film and the two-step reduction from Fe_3O_4 to Fe. In the subsequent cycles, the plateau at 0.92 V in the discharge process and the big slop at 1.5–2.0 V in the charge process correspond to the electrochemical reduction/oxidization ($Fe_3O_4 \leftrightarrow Fe$), matching well with the peaks in CV curves. The Fe_3O_4/C hybrid delivers a high lithium storage capacity of 1630 mA h g^{-1} in the first discharge, based on the total mass of the Fe_3O_4/C hybrid. The first charge capacity is calculated to be 901 mA h g^{-1}, yielding a low initial coulombic efficiency of 55.3%. The capacity loss in the first cycle is attributed to the irreversible consumption of electrolyte and formation of SEI film on the porous surface of Fe_3O_4/C hybrid. In practical application, the low initial coulombic efficiency-

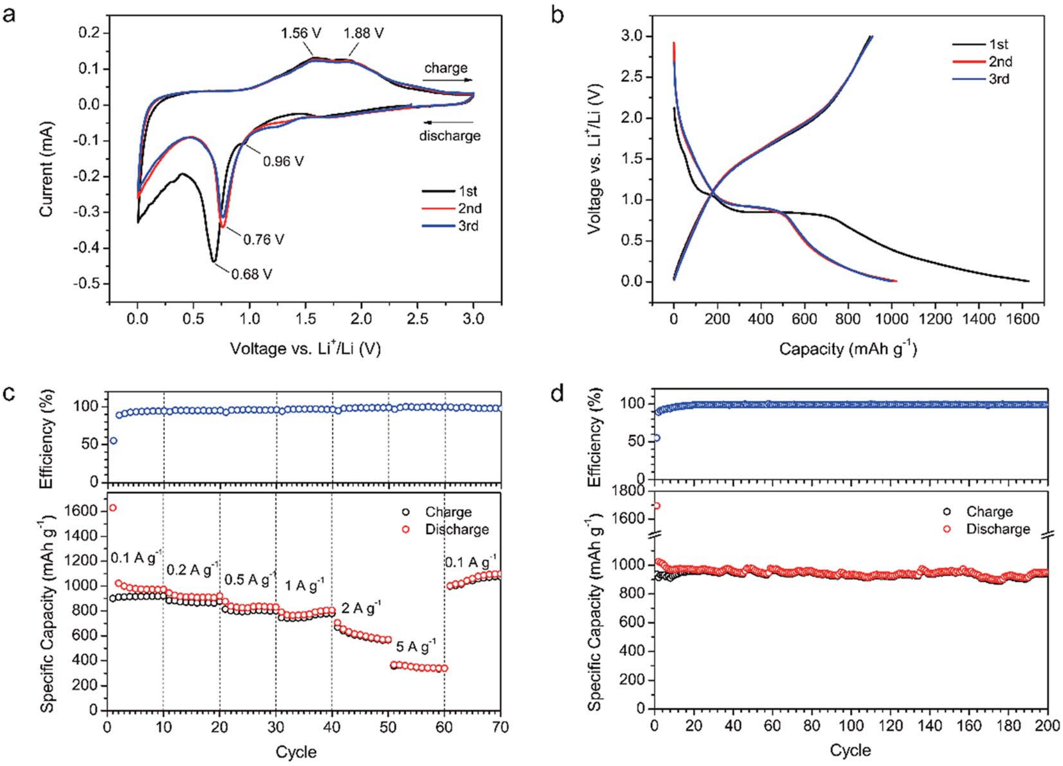

Fig. 4 Electrochemical performance of the Fe_3O_4/C hybrid in LIBs. (a) CV curves. (b) GCD profiles. (c) Rate performance. (d) Cycling performance at 0.1 A g^{-1}.

caused lithium consumption can be solved by a pre-lithiation treatment of electrodes.

Fig. 4c shows the rate performance and corresponding coulombic efficiency of the Fe_3O_4/C based LIBs at various current densities ranging from 0.1 to 5 A g^{-1}. During the first ten cycles at 0.1 A g^{-1}, the discharge capacity decays from 1630 mA h g^{-1} in the first cycle, to 1022 mA h g^{-1} in the second cycle, and then gradually to 974 mA h g^{-1} in the tenth cycle. This gradual capacity decay corresponds to the continuous yet gradually ceasing SEI growth on the surfaces of the Fe_3O_4 and carbon matrix.[59] The discharge capacities of Fe_3O_4/C hybrid at 0.1, 0.2, 0.5, 1, 2 and 5 A g^{-1}, are calculated to be 973, 920, 832, 805, 570 and 339 mA h g^{-1}, in the 10th, 20th, 30th, 40th, 50th and 60th cycles, respectively. As the current density returned to the initial value of 0.1 A g^{-1} in the 61st cycle, a capacity of 1002 mA h g^{-1} is still recoverable and sustainable up to the 70th cycle without any loss (1097 mA h g^{-1} at the 70th cycle). These values are higher than most reported Fe_3O_4-based materials, like 3D Fe_3O_4@GS/GF,[34] GF@Fe_3O_4,[35] Fe_3O_4@mC,[42] G-Fe_3O_4-GNRs,[43] and G-Fe_3O_4@C,[60] as summarized in Table S1.† The high specific capacity and excellent rate performance of our Fe_3O_4/C are ascribed to the nano size of active Fe_3O_4 ($\sim$5 nm), rational mesoporous channels and abundant graphitic electron pathways in the carbon matrix. First, the nanosized Fe_3O_4 can provide high reactive surface area for the Li^+/Li reactions. Second, the short surface-to-core distance of nanosized Fe_3O_4 can facilitate the diffusion of Li^+. Third, the sufficient and rational mesopore channels can provide efficient transportation paths for electrolyte ions even at high current densities. Fourth, the abundant graphitic carbons can facilitate the transportation of electrons. Thus, high capacities and excellent rate performance are obtained.

Fig. 4d shows the cycling performance of the Fe_3O_4/C-based LIBs at 0.1 A g^{-1}. After a slight decrease in the first ten cycles, the Fe_3O_4/C hybrid shows stable cyclic performance with a capacity retention of 952 mA h g^{-1} in the 200th cycle, which is 98% of the 10th capacity (972 mA h g^{-1}). The high specific capacity over the theoretical value of Fe_3O_4 (926 mA h g^{-1}) and carbon (372 mA h g^{-1} for graphite and 744 mA h g^{-1} for graphene) in the hybrid are mainly attributed to three factors. First, the large surface area of the hierarchical porous carbon matrix and nanosized Fe_3O_4 can attribute to the lithium storage through surface adsorption.[58,61] Second, the functional groups on the surface of the hybrid can provide additional faradic capacity. Third, the reversible decomposition of the electrolyte with the formation of SEI and extra lithium ion adsorption/desorption on the SEI during cycling may also offer lithium storage capacity.[58] During cycling, the corresponding coulombic efficiency quickly increases from the initial 55–98% in the 15th cycles, and then maintains high values *ca.* 99% in the following cycles, revealing the high reversible conversion reactions between the nanosized Fe_3O_4 and Li^+. The high reversibility and excellent cycling stability is attributed to the robust and integrated microstructure of Fe_3O_4/C hybrid. Generally, Fe_3O_4 particles suffers from large volume expansion during charge–discharge cycling accompanying by large strain and stress, leading to the pulverization of electrodes and the decrease in capacity during cycling. In our Fe_3O_4/C hybrid, the Fe_3O_4 nanoparticles are firstly wrapped by few layers of graphitic carbons and then well-embedded in the robust and interconnected carbon branches. The volume change-induced strain and stress can be well buffered by the dual protection of carbons, thus avoiding the pulverization of electrode and leading to an excellent cyclic performance. The microstructure comparison of the Fe_3O_4/C before and after cycling are shown in Fig. 5. After 200 cycles at 0.1 A g^{-1}, the size of Fe_3O_4 nanoparticles expands from the initial 5 nm to 8–10 nm (Fig. 5c and f), while the morphology of Fe_3O_4 tends to change from solid to hollow (Fig. 5b and e). Despite of the distinct volume expansion, the expanded Fe_3O_4 nanoparticles are still uniformly embedded in the carbon matrix (Fig. 5d), demonstrating the robust microstructure of our Fe_3O_4/C hybrid. In a full LIB, to match with the cathode, the high capacity of the Fe_3O_4/C (974 mA h g^{-1} *vs.* 372 mA h g^{-1} for commercial graphite anode) may contribute to less weight of anode, but the high delithiation potential (∼1.5 V *vs.* ∼0.1 V for graphite) would lead to the reduction of discharge voltage, which is a common disadvantage for metal oxides/sulfides-based anodes. In the future, with the development of high-voltage cathode materials (*e.g.*, 5 V or above), the disadvantage of high delithiation potential would be suppressed and the advantage of high specific capacity would win out and lead to higher energy density.

3.3. Electrochemical performance of the NIBs

Since the conversion reaction between Fe_3O_4 and Li^+ is similar to that between Fe_3O_4 and Na^+, and the mesoporous channels of the Fe_3O_4/C hybrid are big enough for Na^+ insertion/extraction, the electrochemical performance of the Fe_3O_4/C hybrid was also measured as the anode of NIBs. The corresponding electrochemical performance in NIBs is shown in Fig. 6. Fig. 6a shows the first three CV curves at a scan rate of 0.1 mV s^{-1} within the voltage window of 0.005–3 V. Compared with the CV peaks for LIBs, the CV peaks for NIBs are much weaker and broader due to the sluggish diffusion of sodium ions.[40] The broad peaks at 1.15 and 0.55 V in the first discharge are attributed to the formation of SEI film, as well as the two-step transition from Fe_3O_4 to Fe (step 1, $Fe_3O_4 + 2Na^+ + 2e^- \rightarrow Na_2(Fe_3O_4)$; and step 2, $Na_2(Fe_3O_4) + 6Na^+ + 6e^- \rightarrow 4Na_2O + 3Fe$). In the following cycles, the reduction peaks at 0.70 V correspond to the conversion from Fe_3O_4 to Fe. The oxidization peaks at 0.75 and 1.30 V are related to the transition from Fe to Fe_3O_4. There are also sharp reduction peaks near 0.1 V and broad oxidation peaks near 0.2 V, corresponding to the Na insertion/extraction in graphitic layers. Fig. 6b shows the GCD profiles of the first three cycles at 0.05 A g^{-1} in the voltage window of 0.005–3 V. The voltages increase and decrease smoothly without apparent plateaus, which is in accordance with the weak and broad CV peaks. The Fe_3O_4/C hybrid exhibits an initial discharge capacity of 1161 mA h g^{-1} and charge capacity of 321 mA h g^{-1}, with coulombic efficiency of 27.6%. Such low initial coulombic efficiency is mainly attributed to the SEI film formation on the large surface area of Fe_3O_4/C hybrid and the electrolyte decomposition.

Fig. 6c shows the rate performance and corresponding coulombic efficiency at various current densities from 0.05 to 5 A g^{-1}. During the first ten cycles at 0.05 A g^{-1}, the discharge

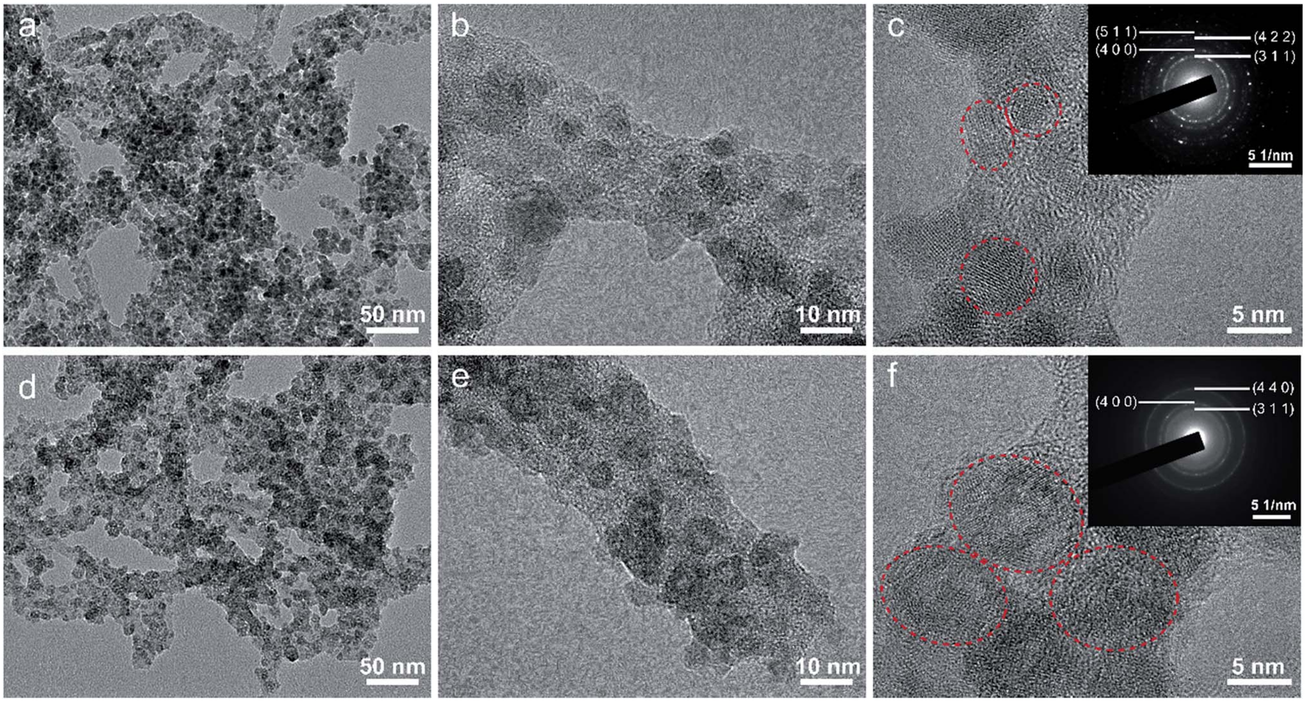

Fig. 5 Microstructural comparison of the Fe_3O_4/C hybrid before and after 200 cycles at 0.1 A g^{-1} in LIBs. (a–c) TEMs before cycling. (d–f) TEMs after cycling.

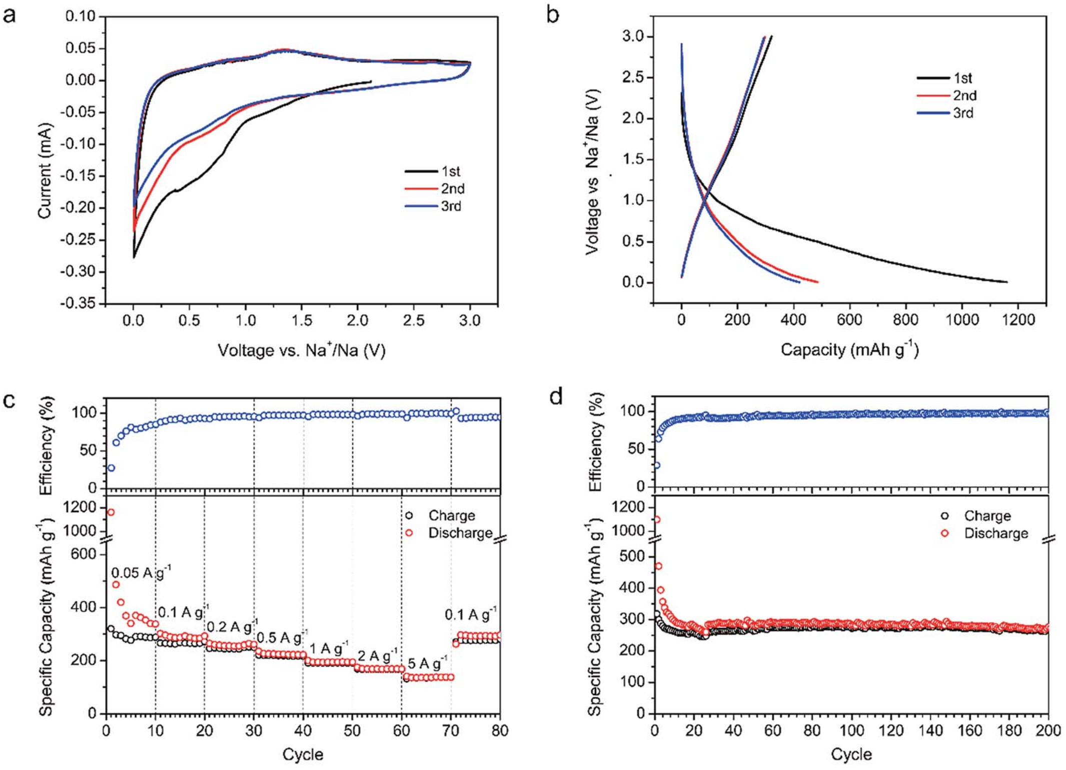

Fig. 6 Electrochemical performance of the Fe_3O_4/C hybrid in NIBs. (a) CV curves. (b) GCD profiles. (c) Rate performance. (d) Cycling performance at 0.1 A g^{-1}.

capacity decays from 1161 mA h g^{-1} in the first cycle, to 487 mA h g^{-1} in the second cycle, and then gradually to the 339 mA h g^{-1} in the tenth cycle, which is caused by the gradual formation of SEI film. The discharge capacities of the Fe_3O_4/C electrode at the current density of 0.05, 0.1, 0.2, 0.5, 1, 2 and 5 A g^{-1} are calculated to be 339, 293, 262, 223, 195, 169 and 138 mA h g^{-1}, respectively, in the 10th, 20th, 30th, 40th, 50th, 60th and 70th cycles. When the current density returns to 0.1 A g^{-1}, a reversible capacity of 295 mA h g^{-1} is recovered, showing a good rate performance. Similar to the situation in LIBs, such good rate performance and relatively high specific capacity are attributed to the nano-sized Fe_3O_4, rational mesoporous channels and abundant graphitic electron pathways in the carbon matrix.

Fig. 6d shows the cycling performance of the Fe_3O_4/C hybrid in NIBs at current density of 0.1 A g^{-1}. The fast capacity loss in the first ten cycles is ascribed to the gradual formation of SEI film, as we have discussed above. In the latter 190 cycles, the capacity remains stable with little decay. The discharge capacity at the 200th cycle is 277 mA h g^{-1}, which is 93.5% of the 10th discharge capacity (296 mA h g^{-1}), indicating an excellent cycling stability. As we have discussed in LIBs, such good cycling stability in NIBs is also attributed to the robust and integrated microstructure of Fe_3O_4/C. The microstructure of Fe_3O_4/C hybrid after 200 cycles in NIBs were also measured by the TEM, as shown in Fig. 7. Unlike in LIBs, the Fe_3O_4 nanoparticles don't have apparent volume expansion after cycling in NIBs, indicating the less intense reaction between Fe_3O_4 and sodium. After 200 cycles, the nanosized Fe_3O_4 are still uniformly embedded in the branch-like carbon frameworks, demonstrating the physical stability of the hybrid structure.

The rate performance and cyclic capability of our Fe_3O_4/C-based NIBs are better than most other Fe_3O_4-based materials, like RGO/Fe_3O_4,[62] C/Fe_3O_4 embedded on CNTs,[63] Fe_3O_4 nanoparticles,[64] and Fe_3O_4/graphene,[65] as summarized in Table S2.† However, the specific capacities of the Fe_3O_4/C in NIBs are much lower than the corresponding values in LIBs. This is a usual phenomenon for most dual-role anode materials.[40,66–70] The phenomenon is mainly caused by the poor kinetics of the sodiation/desodiation processes.[40] To verify this, EIS of the Fe_3O_4/C-based LIBs and NIBs were measured with a frequency range of 10 mHz to 100 kHz and ac amplitude of 10 mV after three CV cycles. Fig. 8 shows the Nyquist plots of the Fe_3O_4/C electrode in LIBs and NIBs. The spectra are fitted based on the equivalent circuit in Fig. S1† and the detailed kinetic parameters are listed in Table S3.† In the high frequency region, the intersection of the plot at real part Z' corresponds to the electrical connection resistance of cells (R_s). In the medium frequency region, the diameter of the semicircle indicates the charge-transfer resistance at the electrode/electrolyte interface (R_{ct}). It is obvious that the charge-transfer resistance in NIBs are much larger than that in LIBs (the fitted R_{ct} for NIBs and LIBs are 445.8 Ω and 162.6 Ω, respectively). This indicates that the Na^+ insertion from the electrolyte to electrode is much slower than Li^+ insertion. In the low frequency region, the slope of the curves corresponds to the diffusive resistance of electrolyte ions

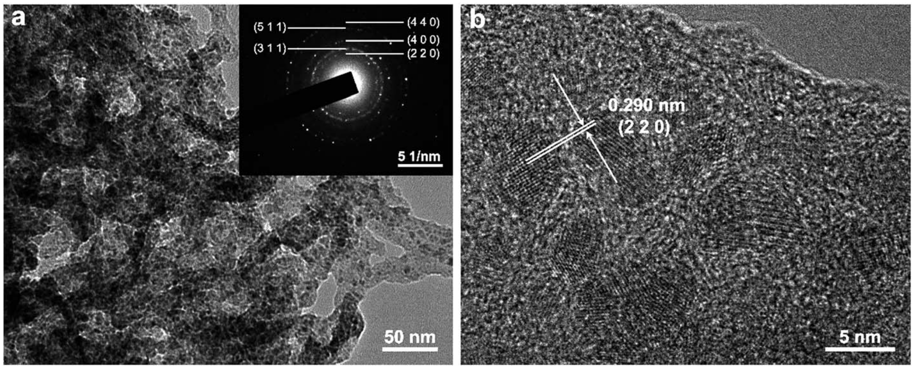

Fig. 7 Microstructure of the Fe_3O_4/C hybrid after 200 cycles at 0.1 A g^{-1} in NIBs. (a) TEM and SAED (inset). (b) HR-TEM.

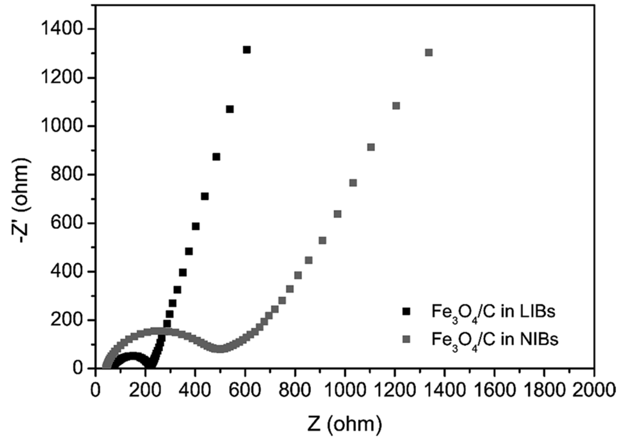

Fig. 8 The Nyquist plots of the Fe_3O_4/C electrodes in LIBs and NIBs.

inside electrode materials (Z_w, Warburg impedance). The slope of Fe_3O_4/C in LIBs is higher than in NIBs, indicating that Li^+ suffers lower impedance during diffusion and reactions inside electrodes compared to Na^+. Thus, the EIS proves that Na^+ insertion/extraction in Fe_3O_4/C-based electrode bears larger impedance and poorer kinetics compared with Li^+, resulting in a lower capacity in NIBs at the same scan rate than in LIBs.

4. Conclusions

In summary, we have demonstrated the effective role of a 3D integrated branch-like Fe_3O_4/C nanostructure in alleviating the volume change and stress problems of Fe_3O_4 during Li^+/Na^+ insertion/extraction. The unique nanostructure is synthesized through a simple carbonization of self-crosslinked Fe-alginate. The obtained Fe_3O_4/C nanohybrid owns ultrafine Fe_3O_4 particle size, mesoporous channels, partially graphitized carbons, and especially a unique integrated branch-like nanostructure. When applied in the anodes of LIBs and NIBs, the ultrafine Fe_3O_4 particle size can help generate high specific capacities, the mesoporous channels and appropriate degree of graphitization can help improve the rate performance, and the robust 3D integrated branch-like structure can well buffer the volume expansions and stresses to keep a physically structural stability and lead to an excellent cyclic stability. With regard to the facile synthesis, excellent electrochemical performance and renewable raw materials, the Fe_3O_4/C hybrids are of great promise for the practical anode materials of LIBs and NIBs.

Conflicts of interest

There are no conflicts to declare.

Acknowledgements

This work was supported by National Key R&D Program of China (2017YFB1201005), National Natural Science Foundation of China (No. 51772187, 51572169), Shanghai Science and Technology Committee (17ZR1441400, 15ZR1422400, 16520710900), and Baotou-SJTU Materials Research Institute. We also thank SJTU Instrument Analysis Centre for the measurements.

References

1 J. B. Goodenough and K.-S. Park, *J. Am. Chem. Soc.*, 2013, **135**, 1167–1176.
2 V. Etacheri, R. Marom, R. Elazari, G. Salitra and D. Aurbach, *Energy Environ. Sci.*, 2011, **4**, 3243–3262.
3 B. Kang and G. Ceder, *Nature*, 2009, **458**, 190–193.
4 C. Zhang, W. Lv, Y. Tao and Q. H. Yang, *Energy Environ. Sci.*, 2015, **8**, 1390–1403.
5 H. Y. Kang, Y. C. Liu, K. Z. Cao, Y. Zhao, L. F. Jiao, Y. J. Wang and H. T. Yuan, *J. Mater. Chem. A*, 2015, **3**, 17899–17913.
6 Y. C. Liu, N. Zhang, L. F. Jiao and J. Chen, *Adv. Mater.*, 2015, **27**, 6702–6707.
7 J. C. Wang and S. Kaskel, *J. Mater. Chem.*, 2012, **22**, 23710–23725.
8 L. H. Yu, N. Brun, K. Sakaushi, J. Eckert and M. M. Titirici, *Carbon*, 2013, **61**, 245–253.
9 N. Brun, K. Sakaushi, J. Eckert and M. M. Titirici, *ACS Sustainable Chem. Eng.*, 2014, **2**, 126–129.
10 W. Nickel, M. Oschatz, S. Rico-Frances, S. Klosz, T. Biemelt, G. Mondin, A. Eychmuller, J. Silvestre-Albero and S. Kaskel, *Chem.–Eur. J.*, 2015, **21**, 14753–14757.

11 L. L. Kong, Z. Zhang, Y. Z. Zhang, S. Liu, G. R. Li and X. P. Gao, *ACS Appl. Mater. Interfaces*, 2016, **8**, 31684–31694.
12 L. P. Ding, S. L. He, S. D. Miao, M. R. Jorgensen, S. Leubner, C. L. Yan, S. G. Hickey, A. Eychmuller, J. Z. Xu and O. G. Schmidt, *Sci. Rep.*, 2014, **4**, 4647.
13 M. H. Wang, H. Yang, X. L. Zhou, W. Shi, Z. Zhou and P. Cheng, *Chem. Commun.*, 2016, **52**, 717–720.
14 D. H. Yang, X. L. Zhou, M. Zhong, Z. Zhou and X. H. Bu, *ChemNanoMat*, 2017, **3**, 252–258.
15 F. Cheng, Z. Tao, J. Liang and J. Chen, *Chem. Mater.*, 2008, **20**, 667–681.
16 X. P. Han, F. Y. Cheng, C. C. Chen, Y. X. Hu and J. Chen, *Nano Res.*, 2015, **8**, 156–164.
17 Y. X. Hu, T. R. Zhang, F. Y. Cheng, Q. Zhao, X. P. Han and J. Chen, *Angew. Chem., Int. Ed.*, 2015, **54**, 4338–4343.
18 S. Li, C. Cheng, H. W. Liang, X. L. Feng and A. Thomas, *Adv. Mater.*, 2017, **29**, 1700707.
19 T. Szatkowski, M. Wysokowski, G. Lota, D. Peziak, V. V. Bazhenov, G. Nowaczyk, J. Walter, S. L. Molodtsov, H. Stocker, C. Himcinschi, L. Petrenko, A. L. Stelling, S. Jurga, T. Jesionowskia and H. Ehrlich, *RSC Adv.*, 2015, **5**, 79031–79040.
20 J. N. Zhang, K. X. Wang, Q. Xu, Y. C. Zhou, F. Y. Cheng and S. J. Guo, *ACS Nano*, 2015, **9**, 3369–3376.
21 D. Tian, X. L. Zhou, Y. H. Zhang, Z. Zhou and X. H. Bu, *Inorg. Chem.*, 2015, **54**, 8159–8161.
22 X. L. Sun, G. P. Hao, X. Y. Lu, L. X. Xi, B. Liu, W. P. Si, C. S. Ma, Q. M. Liu, Q. Zhang, S. Kaskel and O. G. Schmidt, *J. Mater. Chem. A*, 2016, **4**, 10166–10173.
23 T. Jaumann, J. Balach, M. Klose, S. Oswald, J. Eckert and L. Giebeler, *J. Electrochem. Soc.*, 2016, **163**, A557–A564.
24 M. Adam, P. Strubel, L. Borchardt, H. Althues, S. Dorfler and S. Kasker, *J. Mater. Chem. A*, 2015, **3**, 24103–24111.
25 R. G. Mendes, A. Bachmatiuk, B. Buchner, G. Cuniberti and M. H. Rummeli, *J. Mater. Chem. B*, 2013, **1**, 401–428.
26 G. H. Li, H. Yang, F. C. Li, J. Du, W. Shi and P. Cheng, *J. Mater. Chem. A*, 2016, **4**, 9593–9599.
27 M. Zhong, D. H. Yang, C. C. Xie, Z. Zhang, Z. Zhou and X. H. Bu, *Small*, 2016, **12**, 5564–5571.
28 Y. T. Zuo, G. Wang, J. Peng, G. Li, Y. Q. Ma, F. Yu, B. Dai, X. H. Guo and C. P. Wong, *J. Mater. Chem. A*, 2016, **4**, 2453–2460.
29 Y. Yang, J. Q. Li, D. Q. Chen and J. B. Zhao, *ACS Appl. Mater. Interfaces*, 2016, **8**, 26730–26739.
30 Y. Wang, Q. T. Qu, Y. Y. Han, T. Gao, J. Shao, Z. C. Zuo, W. J. Liu, Q. Shi and H. H. Zheng, *J. Mater. Chem. A*, 2016, **4**, 10314–10320.
31 J. Liu, X. J. Xu, R. Z. Hu, L. C. Yang and M. Zhu, *Adv. Energy Mater.*, 2016, **6**, 1600256.
32 J. Q. Jiao, W. D. Qiu, J. G. Tang, L. P. Chen and L. Y. Jing, *Nano Res.*, 2016, **9**, 1256–1266.
33 C. Ding, Y. W. Zeng, L. L. Cao, L. F. Zhao and Y. Zhang, *J. Mater. Chem. A*, 2016, **4**, 5898–5908.
34 W. Wei, S. B. Yang, H. X. Zhou, I. Lieberwirth, X. L. Feng and K. Mullen, *Adv. Mater.*, 2013, **25**, 2909–2914.
35 J. S. Luo, J. L. Liu, Z. Y. Zeng, C. F. Ng, L. J. Ma, H. Zhang, J. Y. Lin, Z. X. Shen and H. J. Fan, *Nano Lett.*, 2013, **13**, 6136–6143.
36 C. N. He, S. Wu, N. Q. Zhao, C. S. Shi, E. Z. Liu and J. J. Li, *ACS Nano*, 2013, **7**, 4459–4469.
37 S. K. Behera, *Chem. Commun.*, 2011, **47**, 10371–10373.
38 S. Zhu, A. C. Marschilok, E. S. Takeuchi, G. T. Yee, G. Wang and K. J. Takeuchi, *J. Electrochem. Soc.*, 2010, **157**, A1158–A1163.
39 L. Liu, H. Zhang, S. W. Liu, H. M. Yao, H. Q. Hou and S. L. Chen, *Electrochim. Acta*, 2016, **219**, 356–362.
40 S. Liu, Y. Wang, Y. Dong, Z. Zhao, Z. Wang and J. Qiu, *ChemElectroChem*, 2016, **3**, 38–44.
41 J. Z. Wang, C. Zhong, D. Wexler, N. H. Idris, Z. X. Wang, L. Q. Chen and H. K. Liu, *Chem.–Eur. J.*, 2011, **17**, 661–667.
42 Y. Chen, B. H. Song, M. Li, L. Lu and J. M. Xue, *Adv. Funct. Mater.*, 2014, **24**, 319–326.
43 L. Li, A. Kovalchuk, H. L. Fei, Z. W. Peng, Y. L. Li, N. D. Kim, C. S. Xiang, Y. Yang, G. D. Ruan and J. M. Tour, *Adv. Energy Mater.*, 2015, **5**, 1500171.
44 S. N. Pawar and K. J. Edgar, *Biomaterials*, 2012, **33**, 3279–3305.
45 K. Y. Lee and D. J. Mooney, *Prog. Polym. Sci.*, 2012, **37**, 106–126.
46 N. Wang, Q. L. Liu, D. M. Kang, J. J. Gu, W. Zhang and D. Zhang, *ACS Appl. Mater. Interfaces*, 2016, **8**, 16035–16044.
47 A. Ōya and S. Ōtani, *Carbon*, 1979, **17**, 131–137.
48 Y. Li, Q. Liu, D. Kang, J. Gu, W. Zhang and D. Zhang, *J. Mater. Chem. A*, 2015, 21016–21022.
49 B. Fang, M. S. Kim, J. H. Kim, S. Lim and J. S. Yu, *J. Mater. Chem.*, 2010, **20**, 10253–10259.
50 M. S. Kim, B. Z. Fang, J. H. Kim, D. Yang, Y. K. Kim, T. S. Bae and J. S. Yu, *J. Mater. Chem.*, 2011, **21**, 19362–19367.
51 B. Fang, J. H. Kim, M. S. Kim and J. S. Yu, *Acc. Chem. Res.*, 2013, **46**, 1397–1406.
52 Y. L. Xing, Y. J. Wang, C. G. Zhou, S. C. Zhang and B. Z. Fang, *ACS Appl. Mater. Interfaces*, 2014, **6**, 2561–2567.
53 A. Eftekhari and B. Fang, *Int. J. Hydrogen Energy*, 2017, 25143–25165.
54 M.-S. Balogun, Y. Luo, W. Qiu, P. Liu and Y. Tong, *Carbon*, 2016, **98**, 162–178.
55 N. Zhang, X. P. Han, Y. C. Liu, X. F. Hu, Q. Zhao and J. Chen, *Adv. Energy Mater.*, 2015, **5**, 1401123.
56 M. Sevilla, C. S. Martínez-de Lecea, T. Valdés-Solís, E. Morallón and A. B. Fuertes, *Phys. Chem. Chem. Phys.*, 2008, **10**, 1433–1442.
57 F. Maldonado-Hodar, C. Moreno-Castilla, J. Rivera-Utrilla, Y. Hanzawa and Y. Yamada, *Langmuir*, 2000, **16**, 4367–4373.
58 C. X. Peng, B. D. Chen, Y. Qin, S. H. Yang, C. Z. Li, Y. H. Zuo, S. Y. Liu and J. H. Yang, *ACS Nano*, 2012, **6**, 1074–1081.
59 Z.-L. Yu, S. Xin, Y. You, L. Yu, Y. Lin, D.-W. Xu, C. Qiao, Z.-H. Huang, N. Yang, S.-H. Yu and J. B. Goodenough, *J. Am. Chem. Soc.*, 2016, **138**, 14915–14922.
60 L. Zhao, M. M. Gao, W. B. Yue, Y. Jiang, Y. Wang, Y. Ren and F. Q. Hu, *ACS Appl. Mater. Interfaces*, 2015, **7**, 9709–9715.

61 Z. S. Wu, W. C. Ren, L. Wen, L. B. Gao, J. P. Zhao, Z. P. Chen, G. M. Zhou, F. Li and H. M. Cheng, *ACS Nano*, 2010, **4**, 3187–3194.

62 S. Zhang, W. Li, B. Tan, S. Chou, Z. Li and S. Dou, *J. Mater. Chem. A*, 2015, **3**, 4793–4798.

63 D.-Y. Park and S.-T. Myung, *ACS Appl. Mater. Interfaces*, 2014, **6**, 11749–11757.

64 P. R. Kumar, Y. H. Jung, K. K. Bharathi, C. H. Lim and D. K. Kim, *Electrochim. Acta*, 2014, **146**, 503–510.

65 Y. Fu, Q. Wei, X. Wang, G. Zhang, H. Shu, X. Yang, A. C. Tavares and S. Sun, *RSC Adv.*, 2016, **6**, 16624–16633.

66 F. Fu, J. D. Li, Y. Z. Yao, X. P. Qin, Y. B. Dou, H. Y. Wang, J. K. Tsui, K. Y. Chan and M. H. Shao, *ACS Appl. Mater. Interfaces*, 2017, **9**, 16194–16201.

67 Z. H. Bi, M. P. Paranthaman, P. A. Menchhofer, R. R. Dehoff, C. A. Bridges, M. F. Chi, B. K. Guo, X. G. Sun and S. Dai, *J. Power Sources*, 2013, **222**, 461–466.

68 X. J. Li, A. L. Hector, J. R. Owen and S. I. U. Shah, *J. Mater. Chem. A*, 2016, **4**, 5081–5087.

69 A. Y. Kim, M. K. Kim, K. Cho, J. Y. Woo, Y. Lee, S. H. Han, D. Byun, W. Choi and J. K. Lee, *ACS Appl. Mater. Interfaces*, 2016, **8**, 19514–19523.

70 S. Hariharan, K. Saravanan, V. Ramar and P. Balaya, *Phys. Chem. Chem. Phys.*, 2013, **15**, 2945–2953.